DEVELOPMENT OF A FLYWHEEL ENERGY STORAGE SYSTEM MODEL IN RSCAD-RTDS AND COMPARISON WITH PSCAD

Document Version
Final published version

Citation for published version (APA):
Vilchis-Rodriguez, D., Preece, R., & Barnes, M. (2023). *DEVELOPMENT OF A FLYWHEEL ENERGY STORAGE SYSTEM MODEL IN RSCAD-RTDS AND COMPARISON WITH PSCAD*. 1-7. Paper presented at PEMD 2023, International Conference on Power Electronics, Machines and Drives, Brussels, Belgium.

Citing this paper
Please note that where the full-text provided on Manchester Research Explorer is the Author Accepted Manuscript or Proof version this may differ from the final Published version. If citing, it is advised that you check and use the publisher's definitive version.

OPEN ACCESS

DEVELOPMENT OF A FLYWHEEL ENERGY STORAGE SYSTEM MODEL IN RSCAD-RTDS AND COMPARISON WITH PSCAD

Damian S Vilchis-Rodriguez[1], Robin Preece[1], Mike Barnes[1]*

[1]*The University of Manchester, Manchester, UK*
**Damian.Vilchis-Rodriguez@manchester.ac.uk*

Keywords: FLYWHEEL, ENERGY STORAGE, RTDS, RSCAD, PSCAD, EMTP

Abstract

In this paper a detailed model of a flywheel energy storage system (FESS) for simulation in the RSCAD-RTDS platform is developed and compared with an implementation developed using the PSCAD-EMTDC program. Grid- and machine-side converter operation is fully considered in the developed model. The operation of the FESS under speed and DC link voltage regulation modes is tested in both platforms. Indirect field-oriented control (FOC) and sinusoidal PWM (SPWM) are considered for the machine control. To enable a direct, fair comparison between the two modelling platforms the PSCAD implementation follows closely the block structure and parameters used in the RSCAD version. The differences between building blocks within each simulation environment are highlighted, and simulation results are compared under charge and discharge operation modes. Contrary to previously published results, good agreement between implementations is obtained when similar parameters and equivalent blocks are used in both environments.

1 Introduction

To allow large scale penetration of renewable, intermittent power sources in the existing energy grid, efficient and effective energy storage devices are required [1, 2]. From existing fast response energy storage technologies, the flywheel energy storage system (FESS) possesses advantageous characteristics in cost, ruggedness, high power density and environmental friendliness. However, its relatively large standby losses compared to other energy storage systems (such as battery, compressed air, and pumped hydro), make the flywheel better suited for applications were frequent charge-discharge is required. [1-3] Furthermore, a FESS can be reliably deeply discharged, for an almost unlimited number of cycles, which is desirable property in voltage regulation and power conditioning applications [3]. A FESS is usually comprised of a rotating machine, a back-to-back, bidirectional power converter and associated control [1-3]. The FESS converts electric energy to be stored in the form of kinetic energy in the associated rotating machine. The amount of energy stored in the device varies linearly with the flywheel mass, and quadratically with its rotational speed. Thus, depending on the application requirements, high and low speed flywheel designs exist [1-4]. Compared to a high-speed design, a low-speed flywheel has the advantage on the use of proven technologies and a substantially lower cost [4]. However, due to the quadratic relationship between stored energy and speed, a low-speed FESS usually exhibits a lower energy density than a high-speed design. Nevertheless, for bulk energy storage, several FESS can be operated in parallel if required.

Energy storage devices are expected to be widely distributed within the energy grid. Therefore, simplified models are usually employed in power system analysis. Furthermore, due to computing resource constraints, the use of dozens of highly detailed models can be unpractical for many applications, such as real time simulations. However, notwithstanding the application, for validation purposes the development of detailed FESS models is also desirable. The RSCAD-RTDS digital simulation platform is commonly used for real-time simulation applications [5]. However, it has been reported that significant differences may exist between RSCAD and equivalent offline EMTP-Type simulations – for example with PSCAD-EMTDC software – when RSCAD's universal converter model (UCM) is considered [6]. Incidentally, power electronic converters are an essential component of a FESS. Owing to the reported differences, a thorough comparison between implementations in both platforms is desirable.

In this paper, a detailed model of a FESS is developed for the RSCAD-RTDS and PSCAD-EMTDC modelling environments. A low-speed flywheel, driven by an induction motor is considered in the test systems and back-to-back two-level voltage source converters (VSCs) are used to interface the machine to a three-phase, AC voltage source. Special attention is paid to the differences between platforms on the component's parameters to allow a fair, direct comparison between modelling environments.

2. Test system description and model implementation

In this research work RSCAD FX 1.4 and PSCAD 5.0.1 are employed for the model development. RSCAD is designed to work in conjunction with the RTDS hardware for real-time based simulations, while PSCAD is a widely used software for offline (non-real-time) EMTP-Type analysis. Both platforms use the EMTP algorithm [7] for the system solution. Therefore, it would be expected that both systems would provide similar

results for the same system and identical time-step. However, significant differences have been reported to exists when power electronics devices are considered [6].

2.1 FESS topology

The FESS test system considered in this work is comprised of the converter transformer, back-to-back VSC two-level converters, and a 2200 HP induction machine. The flywheel is considered as a rigid, additional single mass attached to the induction machine. Fig. 1 shows a schematic representation of the system considered in this work and the parameters of the machine are listed in Table I.

Indirect field-oriented control (FOC) [9], and sinusoidal PWM (SPWM) are used in the model. SPWM was preferred to allow the use of the inbuilt RSCAD firing pulse and universal two-level converter blocks combination (rtds_ss_UCM_FP and rtds_ss_UCM_LEV2, respectively), such components are shown in Fig. 2 for reference. The improved (high precision) firing pulse option was used for the RSCAD converter-firing pulse blocks combination. Using the Improved Firing input, the performance of the UCM is expected to be equivalent to that of the PSCAD software [10]. It should be noted that converter terminal reactor and valves snubber circuits are part of the RSCAD UCM block and cannot be disabled. Therefore, for consistency, such components were also included in the PSCAD implementation. The back-to-back converter and SPWM were built in PSCAD using discrete components, this is illustrated in Fig. 3. To minimize any discrepancy in the simulation results between platforms, particular care was taken to use the same parameter values in both implementations. The valve/diode forward voltage drop is not included as an option for RSCAD's UCM block, therefore such value was set to zero for PSCAD diode/IGBT pairs. A $1m\Omega$ ON resistance was assumed.

To enable the simulation of the FES system in PSCAD, the connection of a high impedance, snubber circuit, to the machine terminals was required (the resulting circuit is shown in Fig. 4). If no snubber is connected, a non-standard error message was triggered, and the simulation cannot be continued. It should be noted that snubber circuits are often required to interface dq based models in EMTP-type simulation programs [11], thus the need for such a connection was somewhat expected. No additional snubber circuit was required to run the RSCAD simulation, since for the purpose of numerical stability, the machine terminals are connected using 300 pu un−compensated shunt connected resistances [12]. Nevertheless, a shunt resistor was also added to the machine terminals in the RSCAD implementation to preserve the equivalence between models, as shown Fig. 5. The addition of the snubber circuit to the RSCAD implementation was found to have a negligible effect on the simulation results.
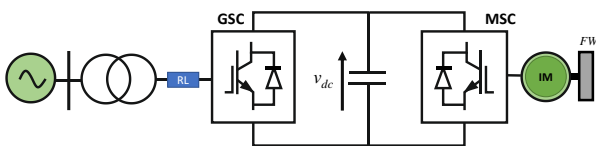

Fig. 1 FESS system schematic diagram.

Table 1 3-phase, 4-Pole, 60Hz, 2250HP, induction machine parameters [8].

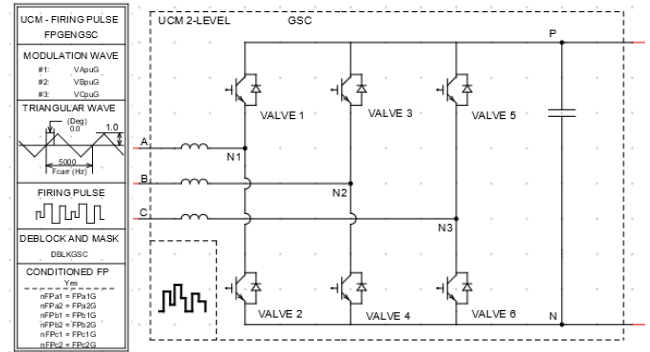| Volt. [V]	Speed [rpm]	r_s [Ω]	x_{ls} [Ω]	x_M [Ω]	x_{lr} [Ω]	r_r [Ω]	J [kg·m^2]
2300	1786	0.029	0.226	13.04	0.226	0.022	63.87

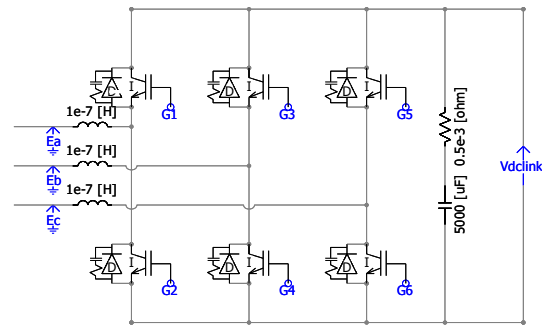Fig. 2 RSCAD firing pulse (left) and UCM (right) blocks.

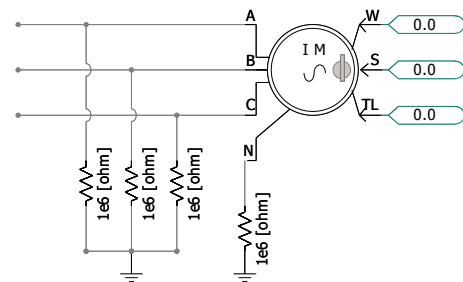Fig. 3 PSCAD grid side converter.

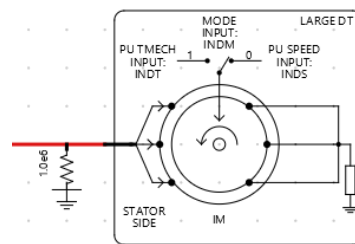Fig. 4 PSCAD induction machine connection.

Fig. 5 RSCAD induction machine connection, single line view.

2

To use the standard induction machine blocks, the machine parameters should be provided in per unit in both platforms. To this end, base quantities were calculated using the machine rated power, voltage and frequency; magnetic saturation was neglected. "Global substitution" and "Draft Variables" were used in PSCAD and RSCAD, respectively, to facilitate the parametrization of the system.

2.1 Machine side converter control

For the machine side converter (MSC), indirect FOC+SPWM is used for the induction machine control. The machine mechanical speed is used to estimate the electrical angle required by the abc-to-dq transformation. Fig. 6 shows a schematic diagram of the implemented control block. The calculation of the variables required by the control algorithm depicted in Fig. 6 is performed using equations (1)-(5) [9, 13].

$$|\psi_r|_{est} = \frac{L_m i_{ds}}{1+\tau_r s} \tag{1}$$

$$i_{qs}^* = \frac{2}{3}\frac{2}{P}\frac{L_r}{L_m}\frac{T_e^*}{|\psi_r|_{est}} \tag{2}$$

$$i_{ds}^* = \frac{|\psi_r|^*}{L_m} \tag{3}$$

$$\theta_e = \int(\omega_m + \omega_s)dt \tag{4}$$

$$\omega_s = \frac{L_m i_{qs}^*}{|\psi_r|_{est}\tau_r} \tag{5}$$

In (1)-(5) $|\psi_r|_{est}$ is the estimated machine flux, L_m is the machine magnetizing inductance, i_{ds} the stator d current, τ_r the rotor time constant, s is the Laplace operator, $i_{qs}*$ the reference stator q-axis current, P the machine pole number, L_r the rotor self-inductance, T_e* the reference electromagnetic torque, $i_{ds}*$ the reference stator d-axis current, $|\psi_r|^*$ the reference machine flux (nominal flux), θ_e the machine electric angle, ω_m the machine rotational speed and ω_s the machine slip speed. The rotor time constant is defined as (6) [9, 13].

$$\tau_r = \frac{L_r}{r_r} = \frac{L_{lr}+L_m}{r_r} \tag{6}$$

In (6) L_{lr} is the rotor leakage inductance and r_r is the rotor phase resistance.

As shown in Fig. 6, depending on the operation mode, the machine control switches between speed and DC voltage regulation modes. During the FESS speeding mode, the reference torque (T_e^*) is derived from the speed outer loop, and the machine is driven to follow a predefined speed profile. During flywheel discharge, the control system switches to DC voltage regulation mode, and the reference torque is then derived from the outer DC voltage loop. This mode of operation implies that only one of the two outer loop PI controllers is effectively active during the system operation. Therefore, to enable the smooth transition from speed to voltage regulation mode, and vice versa, the non-active PI controller is set to zero, while non-operational.
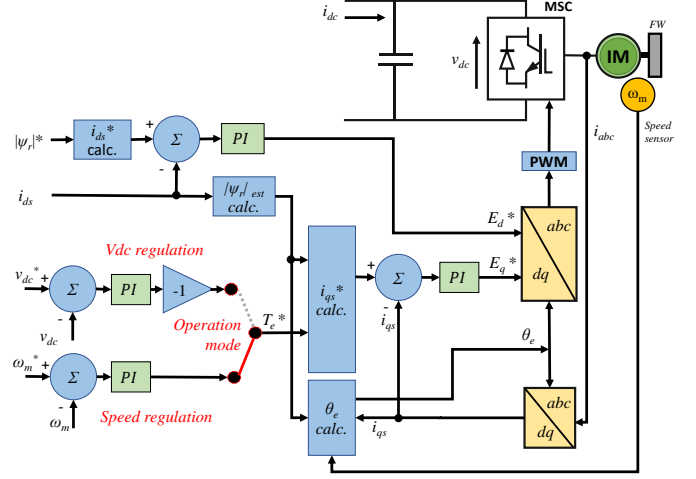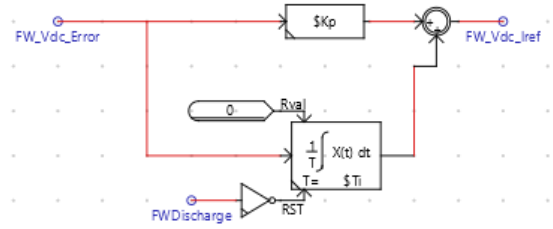

Fig. 6 MSC control block

Fig. 7 RSCAD DC voltage PI controller detail.

The PI controller reset mechanism is illustrated in Fig. 7, where a detailed view of the controller block is shown. As illustrated in the figure, the state of integral component of the PI controller is dictated by the operating mode flag "FWDischarge": when "FWdischarge" is 0, the output of the integrator is set to zero, effectively erasing the error history. For consistency, a similar PI block structure was implemented in PSCAD using discrete components instead of the in-built PI controller block.

As can be seen in Table 1, the induction machine used in the FESS is rated for operation at only 1786 rpm. To enable machine operation above rated speed, flux weakening is considered. Thus, when the machine operates above rated speed, the reference flux is scaled accordingly using (7) [14]. Otherwise, the nominal machine flux is used as the reference flux value.

$$\psi_r = \frac{|\psi_r|^* \omega_{mbase}}{\omega_m} \tag{7}$$

In (7), ω_{mbase} is the machine base angular speed. It should be noted that care should be taken in (7) to avoid division by zero when the machine is at standstill.

2.2 Grid side converter control

The grid side converter (GSC) controller follows the operating principles set forward in [15]. The GSC controller consists of an inner current control loop and an external power control loop, with decoupled active and reactive power control capabilities. Fig. 8 shows a schematic representation of the GSC control block. The AC source in Fig. 8 emulates the connection to the grid. For the investigated FESS application, the

reference reactive power (Q*) is set to zero in the corresponding control loop.

The reference angle required by the GSC dq based controller is derived from the voltages at the point of connection using a PLL, the three-phase enhanced PLL block (_rtds_3phEPLL) is used in RSCAD, while the standard in-built PLL block is used on the PSCAD implementation.

The converter reactor included in the RSCAD's UCM block (and connected at the converter terminals) is considered in the control block by lumped in the series RL circuit (connected between the converter terminals and the 3-phase voltage in Fig. 8) the corresponding resistance and inductance values. As for the MSC controller, previsions for DC link voltage regulation are added to the GSC so that it regulates the DC link voltage during the flywheel charging phase. Alternatively, the GSC delivers the requested power (rated power) when commanded, while the MSC controller regulates the DC link voltage.

As is the case for the MSC, depending on the operation mode (v_{dc} regulation or power regulation) only one of these outer loop PI controllers, shown if Fig. 8, is in operation. This is further illustrated in Fig. 9, where a detail of the RSCAD implementation of the GSC control block is shown. Thus, depending on the value of the "ControlType" flag, power or voltage regulation mode are engaged. For consistency a similar block structure is implemented in PSCAD.
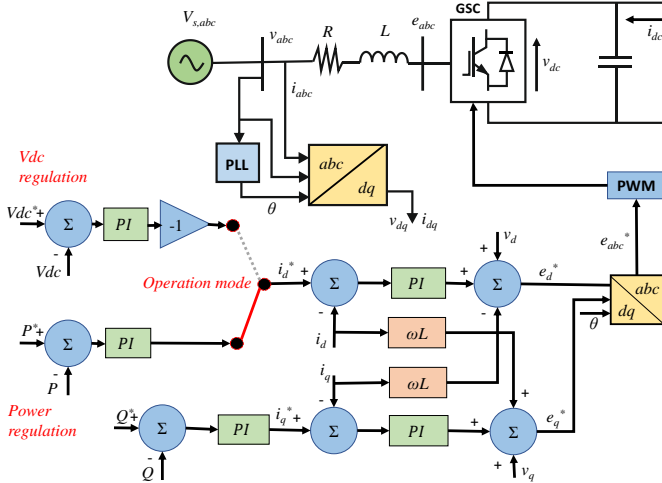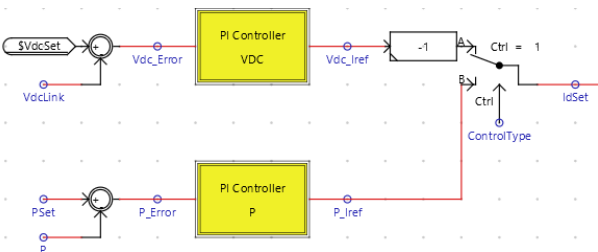

Fig. 8 GSC control block

Fig. 9 RSCAD GSC control block detail.

3   Simulation results

RSCAD FX 1.4 and PSCAD 5.0.1 are employed for the simulations. In the simulations the FESS is connected to a three-phase 13.8 kV, 50 Hz AC voltage source using a 2 MVA, 13.8-2.3 kV, wye-delta transformer. The switching frequency is 5 kHZ, a 4.6 kV DC link voltage, and a 10 mF DC link capacitor are also used with the test system. The FESS is rated to deliver 1 MW, peak power during 4s.

The RSCAD model is run at an RTDS station comprised of two stacks with five PB5 processor cards in each; a single stack is used at run-time. The PSCAD model is run in a Core i7-12700 Windows PC, with 64 GB of RAM.

RSCAD allows the use of multiple time-step sizes (main step, small-step, sub-step, super-step) for different sub-systems within the same simulation (multi-rate simulation), while PSCAD uses a single time step size for the entire solution. For consistency with PSCAD, and to enable a direct comparison, the implementation in RSCAD is conducted in the main step. A small time-step of 1 µs is used in both environments to ensure an accurate solution. It should be noted that for such small time-step, real-time simulation was not achievable with the RTDS hardware configuration employed. Therefore, the non-real-time option was used to run the RSCAD-RTDS simulation. Incidentally, the minimum time-step at which real-time simulation was achievable in the RSCAD-RTDS implementation was 20µs, however considerable error was incurred with such time-step in the two platforms under test. Fig. 10 shows the RSCAD and PSCAD diagrams of the test system.

For comparison, a FESS charge-discharge cycle is considered in this assessment:

- First, the DC link capacitor is charged to the reference voltage using a DC source, while the GSC delivers rated power.
- At 1 s, the DC source is disconnected and the GSC switches to voltage regulation mode.
- At 2 s, the flywheel starts to charge at a constant rate, until it reaches a speed of 400 rad/s at 12 s.
- At 14 s, the GSC is commanded to deliver rated power, and the flywheel switches operation to DC regulation mode.
- Finally, the flywheel delivers rated peak power until the simulation ends at 16 s.

Fig. 11 shows the flywheel speed profile obtained from the PSCAD and RTDS simulations. In the figure 0.16 s were subtracted at the start of the RSCAD simulation to account for the 'pre-trigger' percentage time required by the RSCAD-RTDS plotting system. Figs. 12-14 show simulation results for DC link voltage, GSC power and induction machine stator currents, respectively. Active and reactive power flowing toward the grid is assumed as positive in the simulations.

As can be seen in Figs. 11-14, good agreement exists between systems results. However, minor differences are noted.
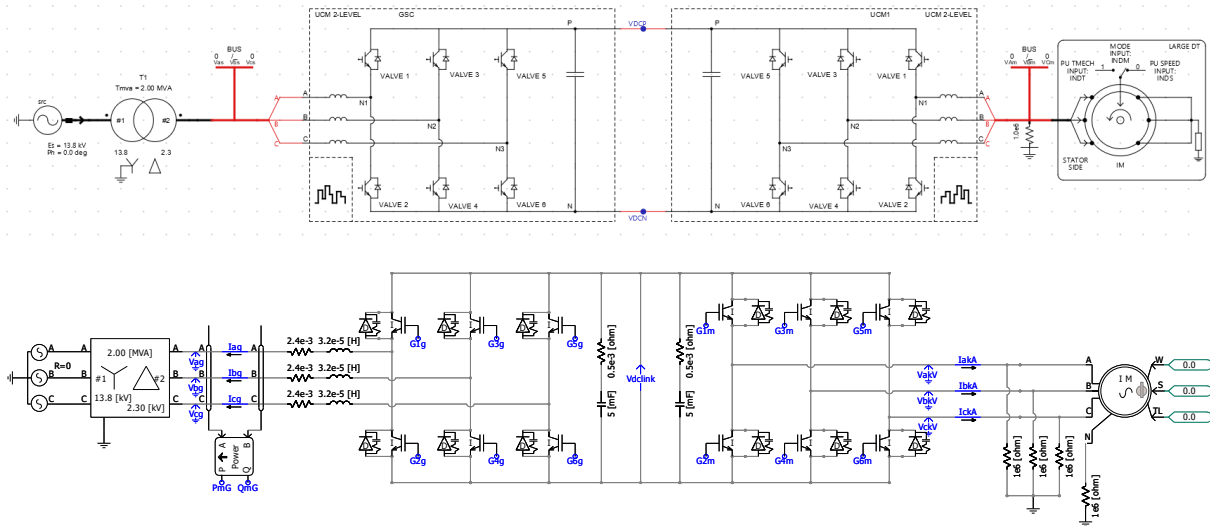
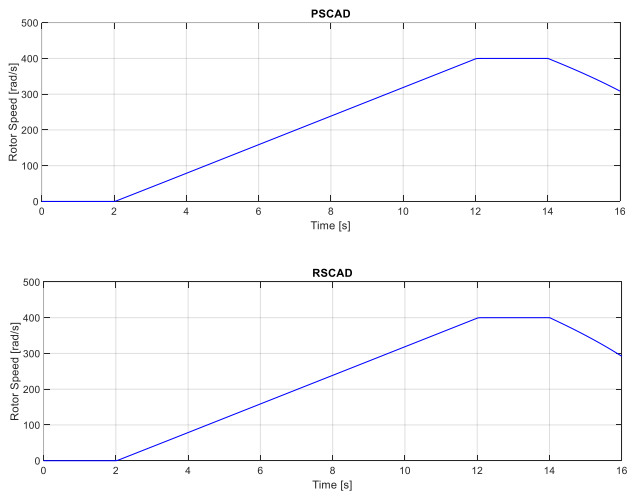Fig. 10 RSCAD (top) and PSCAD (bottom) test FESS circuit diagram.

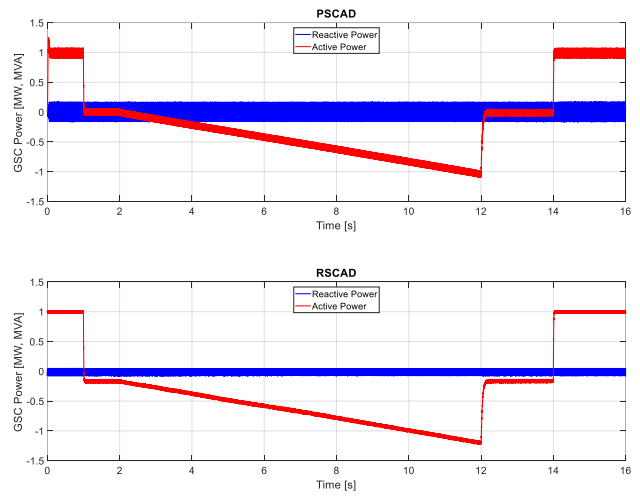Fig. 11 PSCAD (top) and RSCAD (bottom) flywheel speed profile.

Fig. 12 PSCAD (top) and RSCAD (bottom) DC link voltage.

Fig. 13 PSCAD (top) and RSCAD (bottom) power profile at the GSC terminals.

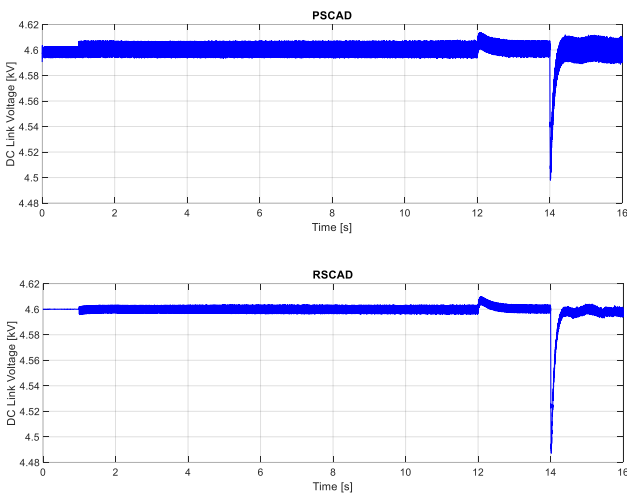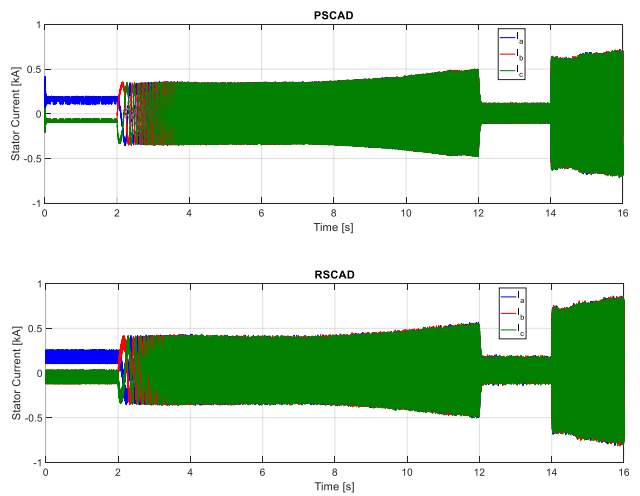Fig. 14 PSCAD (top) and RSCAD (bottom) Induction machine stator currents.

As can be seen in Fig. 11, the final speed of the flywheel is slightly lower in RSCAD that in the PSCAD results: 292 and 308 rad/s, respectively. This is most probably related with the higher active power consumption observed in the RSCAD simulation in Fig. 13. In Fig. 13, there is a noticeable active power consumption (of approximately 120 kW) in RSCAD during the periods where the machine is operating at constant speed (1 to 2 s and 12 to 14 s). The flywheel needs to compensate these losses during operation to deliver the requested 1MW peak power. This is also reflected in differences in the machine current. By comparison, the power consumption in PSCAD is close to zero during these periods. Clearly, there is some additional power flowing from the transformer terminals toward the GSC in the RSCAD implementation. To determinate if the power losses observed in the in RSCAD results in Fig. 13 are associated with the converter operation, equivalence of the induction machine models used in PSCAD and RSCAD was investigated. Fig. 15 shows simulation results, for the induction machine used in the FESS but operating separately from it, with the machine directly connected to an infinite bus. The results show the machine startup transient from standstill, under no load. As shown in Fig. 15, the results from RSCAD and PSCAD are indistinguishable from each other, demonstrating equivalence between machine models. Hence, the additional power consumption observed in the RSCAD simulation in Fig. 13 is almost certainly related to the converter operation.

Also, a minor difference in the DC link voltage dip during flywheel discharge can be observed in the results (Fig. 12): 4498V in PSCAD and 4487V in RSCAD. Another difference between results is the ripple level present in the signals. For instance, the magnitude of the ripple present in the DC link voltage and power signals is slightly larger in PSCAD (12V) than in RSCAD (7V), while the opposite occurs for the current signals. Such high frequency components are usually related to the converter switching frequency. This is illustrated in Fig 16, where the frequency spectrum of the DC link voltage signal obtained from the RSCAD and PSCAD simulations is shown. As shown in Fig. 16, multiple harmonics of the switching frequency are present in the signal spectrum. The sidebands around the harmonics of the switching frequency, at multiples of the fundamental frequency, are predicted to exist in a two-level converter [13]. Consistent with the results in Fig. 12, it is clear in Fig. 16 that the noise floor in the DC link voltage signal is substantially lower in the RSCAD than in the PSCAD results. Thus, although the UCM with improved firing pulse is expected to have similar performance than PSCAD [10], the differences observed between results are most probably related to differences in the way the power electronics components are modelled in both platforms. However, beside the difference in the converter power consumption, the other differences found in the simulation can be considered minor for the analysed case: 16 rad/s in flywheel final speed, 5V in DC voltage ripple and 9V in DC voltage dip. It should be noted that the difference in power consumption is not necessarily an indicative of an incorrect model, but rather an indicative of differences in the assumptions made in the model; further analysis is necessary to identify the root cause of this specific difference.
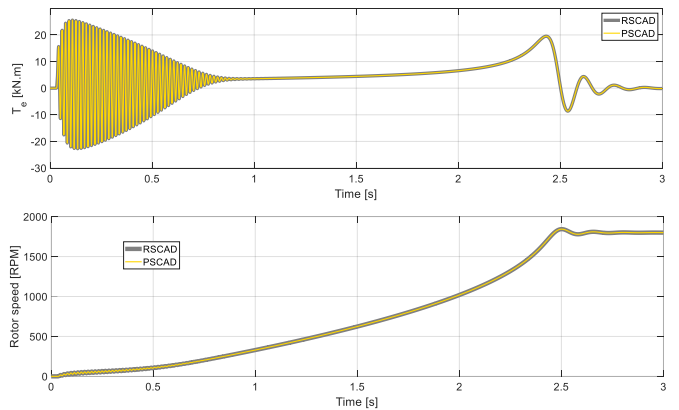

Fig. 15 Induction machine startup simulation results for electromagnetic torque (top) and rotor speed (bottom).
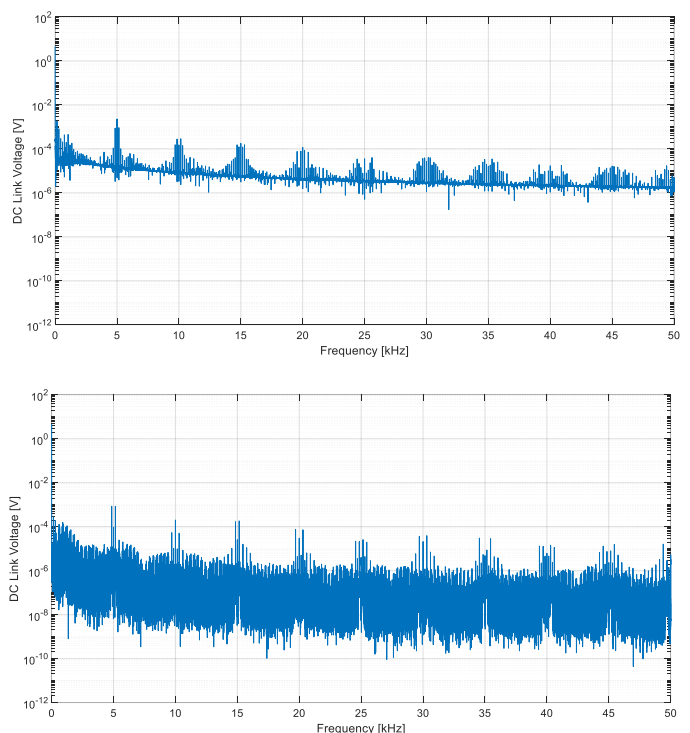

Fig. 16 DC link voltage frequency spectrum: PSCAD (top), RSCAD (bottom).

4 Conclusion

In this paper a FESS was implemented for the RSCAD-RTDS and PSCAD-EMTDC, EMTP-type simulation platforms. Details on the differences between the two platforms components are highlighted. The simulation of a FESS charge-discharge cycle was conducted, and the results were compared. The non-real-time comparison between systems results for a small time-step of 1 µs shows a good agreement between the two solutions. However, differences in standby losses and the level of high frequency oscillations exist. The differences between results are most probably related to the way the FESS converters, and corresponding switching operation, are modelled in both platforms. However, contrary to previous published comparisons, beside the difference in power consumption, the other

differences found can be considered minor: 9V in DC link voltage dip and 5V in DC voltage ripple.

5   Acknowledgements

6   References

[1] Hadjipaschalis, I., Poullikkas, A., Efthimiou, V.: 'Overview of current and future energy storage technologies for electric power applications.' Renewable and Sustainable Energy Reviews, Volume 13, Issues 6–7, 2009, Pages 1513-1522.

[2] Díaz-González, F., Sumper, A., Gomis-Bellmunt, O., Villafáfila-Robles, R.: 'A review of energy storage technologies for wind power applications'. Renewable and Sustainable Energy Reviews, Volume 16, Issue 4, 2012, Pages 2154-2171.

[3] Peña-Alzola, R., Sebastián, R., Quesada, J., Colmenar, A.: 'Review of flywheel based energy storage systems'. 2011 International Conference on Power Engineering, Energy and Electrical Drives, Malaga, Spain, 2011, pp. 1-6.

[4] Gallo, A.B., Simões-Moreira, J.R., Costa, H.K.M., Santos, M.M., Moutinho dos Santos, E.: 'Energy storage in the energy transition context: A technology review'. Renewable and Sustainable Energy Reviews, Volume 65, 2016, Pages 800-822.

[5] 'RSCAD® FX: REAL-TIME SIMULATION SOFTWARE PACKAGE', https://knowledge.rtds.com/hc/en-us/article_attachments/6954305297303/RSCAD_FX_-_Real-Time_Simulation_Software_Package.pdf, accessed 2 June 2023.

[6] Tinajero, G.D.A., Guerrero, J.M., Segundo, J. and Esparza, A.: 'Performance Assessment of the RTDS/RSCAD VSC model'. Journal of Physics: Conference Series. Vol. 1457. No. 1. IOP Publishing, 2020.

[7] Dommel, H.W.: 'Electromagnetic Transient Program (EMTP) Rule Book'. Electro Power Res. Inst., Palo Alto, CA, EPRI EL 642-1, Jun. 1989.

[8] Krause, P. C., Wasynczuk, O., Sudhoff, S.D.: 'Analysis of Electric Machinery and Drive Systems'. Wiley-IEEE Press, 2002.

[9] Hemavathy, K., Pappa, N., Kumar, S.: 'Comparison of indirect vector control and direct torque control applied to Induction Motor drive'. 2014 IEEE International Conference on Advanced Communications, Control and Computing Technologies, Ramanathapuram, India, 2014, pp. 192-197.

[10] 'Introducing the Universal Converter Model for enhanced real-time power electronics simulation', https://www.rtds.com/ucm/, accessed 3 June 2023.

[11] Wang, L. et al.: 'Methods of Interfacing Rotating Machine Models in Transient Simulation Programs'. in IEEE Transactions on Power Delivery, vol. 25, no. 2, pp. 891-903, April 2010.

[12] RTDS Technologies, 'RSCAD Power System components manual', electronic help file.

[13] Feng, J., Gongbao, W., Lijun, F., Yaqiao, Y., Ruitian, W. Zhen, X.: 'Controller design of flywheel energy storage systems in microgrid'. 2014 17th International Conference on Electrical Machines and Systems (ICEMS), Hangzhou, China, 2014, pp. 2821-2826.

[14] Cardenas, R., Pena, R., Asher, G. M., Clare, J. and Blasco-Gimenez, R.: 'Control strategies for power smoothing using a flywheel driven by a sensorless vector-controlled induction machine operating in a wide speed range'. in IEEE Transactions on Industrial Electronics, vol. 51, no. 3, pp. 603-614, June 2004.

[15] Vilchis-Rodriguez, D. S., Ahmedi, A., Barnes, M., Shen, S., Wang, Z. and Gao, S.: 'STATCOM+BESS Modelling and Harmonic analysis'. The 17th International Conference on AC and DC Power Transmission (ACDC 2021), Online Conference, 2021.